Journal of Hepatocellular Carcinoma

Dovepress
Taylor & Francis Group

Open Access Full Text Article

ORIGINAL RESEARCH

MRI Radiomics for Distinguishing HBV-Related Early Hepatocellular Carcinoma from Precancerous Nodules

Jiachen Liu[1], Xiurong Ding[2], Yanyan Zhang[1], Wei Wang[1], Zhongkai Zhou[1], Hongjun Li[1]

[1]Radiology Department, Beijing Youan Hospital, Capital Medical University, Beijing, People's Republic of China; [2]Department of Clinical Laboratory, Beijing Youan Hospital, Capital Medical University, Beijing, People's Republic of China

Correspondence: Hongjun Li, Email lihongjun00113@126.com

Objective: To investigate the predictive value of intratumoral and peritumoral radiomic features from multiparametric MRI in differentiating HBV-associated early hepatocellular carcinoma (eHCC) from precancerous nodules.

Methods: Between January 2019 and October 2024, a total of 133 patients with eHCC and 89 patients with pre-HCC lesions who underwent preoperative MRI were enrolled in the study. Multivariate analysis identified independent predictors for eHCC used to build a clinical prediction model. Radiomics models based on multiphase MRI across multiple tumor regions (entire tumor, Peri_4mm, Peri_6mm, Peri_8mm) were developed. Features from the intratumoral and optimal peritumoral region were combined into an IntraPeri model. A nomogram was developed by combining clinical and IntraPeri model variables. Model performance was evaluated using the area under the curve (AUC).

Results: 222 patients (mean age, 57.2 years ± 11.0; 164 men) were evaluated. DWI hyperintensity, T1WI hypointensity, and a low globulin-to-lymphocyte ratio (GLR) were identified as risk factors for eHCC. 1,409 radiomic features were extracted from each ROI; 27 were retained for analysis and model development. The clinical model achieved AUCs of 0.826 and 0.798 in the training and internal validation cohorts, respectively, while the intratumoral model yielded AUC values of 0.884 and 0.838. The Peri_6mm model outperformed the Peri_8mm and Peri_4mm models. The IntraPeri model demonstrated excellent performance, achieving AUCs of 0.947 and 0.935 in the training and internal validation cohorts, respectively. The comprehensive nomogram demonstrated the highest performance with AUCs of 0.958 and 0.950.

Conclusion: Our study highlights the potential of a multiparametric MRI-based radiomics nomogram that integrates both intratumoral and peritumoral features as an effective tool for differentiating eHCC.

Keywords: early hepatocellular carcinoma, precancerous nodules, magnetic resonance imaging, intratumoral and peritumoral, radiomics

Introduction

Hepatocellular carcinoma (HCC) is the sixth most common cancer worldwide and the third leading cause of cancer-related mortality, accounting for 75–85% of all primary liver malignancies. China accounts for nearly half of the global HCC burden, with approximately 466,000 new cases reported in 2022.[1] Chronic hepatitis B virus (HBV) infection leading to cirrhosis is a major underlying cause of HCC in China, predominantly affecting middle-aged and elderly men.[2] HBV-related HCC develops progressively through distinct stages: from regenerative nodules (RNs) to premalignant dysplastic nodules (LGDNs/HGDNs), then to early HCC (eHCC), and finally advanced HCC.[3] According to the International Liver Tumor Consensus Group and the WHO Digestive System Tumor Classification (2010),[4,5] eHCC is defined as a solitary, well-differentiated tumor ≤2 cm without vascular invasion or metastasis. Studies[6,7] have demonstrated that curative resection for eHCC achieves a 5-year survival rate exceeding 70%, in contrast to advanced HCC, where median survival is limited to 1–2 years. Although eHCC is clearly distinguishable from classical HCC, differentiating it from precancerous lesions (DNs) remains a diagnostic challenge due to its intermediate transitional nature.[8–10]

https://doi.org/10.2147/JHC.S567418
Received: 13 September 2025
Accepted: 31 December 2025
Published: 13 January 2026

Graphical Abstract

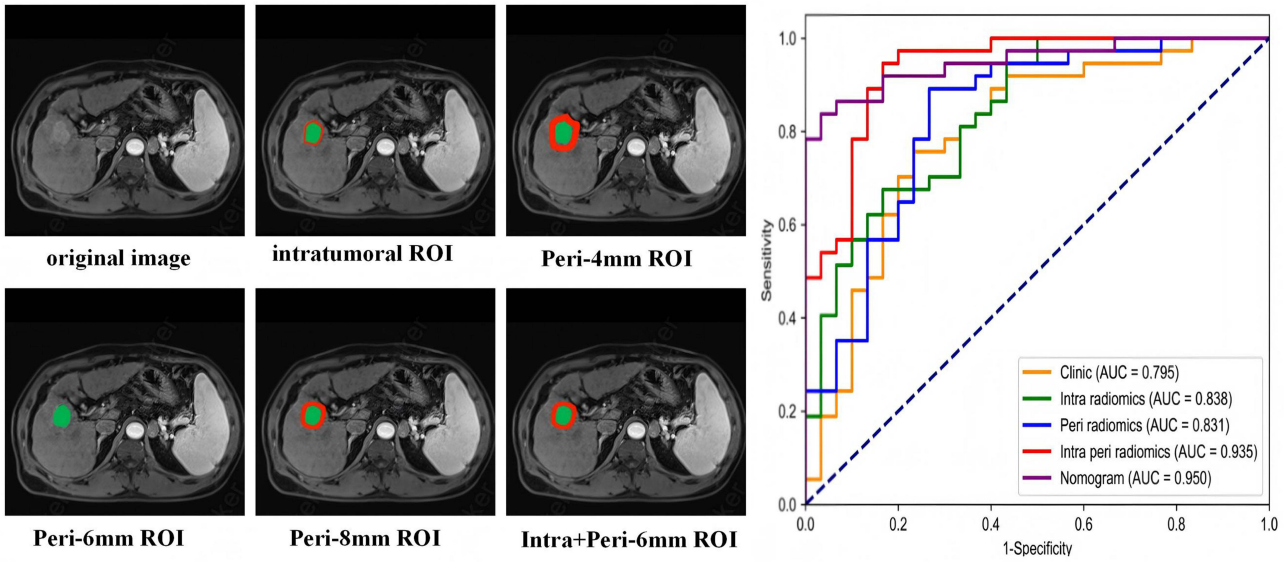

Magnetic Resonance Imaging (MRI) excels in the detection of HCC due to its superior soft-tissue contrast. The combination of Gd-EOB-DTPA-enhanced MRI with diffusion-weighted imaging (DWI) further improves diagnostic accuracy in identifying focal liver lesions, including small HCC and DNs.[11,12] However, the current LI-RADS criteria predominantly depend on arterial phase hyperenhancement and washout appearance—imaging features that are often absent or minimally expressed in eHCC. In contrast, certain HGDNs may exhibit similar atypical enhancement patterns, leading to diagnostic ambiguity in differentiating eHCC from premalignant lesions.[13] This highlights the urgent need for novel diagnostic strategies to enable early lesion detection, which is critical for timely clinical intervention.

Radiomics overcomes the limitations of conventional imaging by extracting high-dimensional quantitative features from medical images. It enables comprehensive analysis of tumor microarchitecture and has shown clinical value in characterizing HCC. MRI-based radiomics studies[14,15] have confirmed its effectiveness in early HCC detection, pathological grading, and predicting microvascular invasion (MVI). However, the majority of current research predominantly focuses on intratumoral features. Emerging evidence[16,17] demonstrates that in eHCC, the peritumoral region extends beyond mere anatomical proximity and functions as a dynamic biological microenvironment that actively contributes to micro-invasion, immune evasion, and pro-angiogenic signaling, thereby influencing tumor progression and clinical outcomes. Studies[18,19] have demonstrated that the integration of intratumoral and peritumoral MRI-derived radiomic features significantly improves diagnostic accuracy in predicting MVI and classifying HCC histopathological subtypes.

Therefore, this study aims to develop and validate a multiparametric MRI-based radiomics model to accurately differentiate eHCC from Pre-HCC, and to evaluate the additional diagnostic value of peritumoral features in enhancing model performance.

Materials and Methods

Patients

This multicenter retrospective study was approved by the Hospital Ethics Committee (LL-2021-019-K), and written informed consent was waived. Between January 2019 and October 2024, a total of 542 patients with focal liver lesions who underwent gadoxetic acid-enhanced MRI examinations were enrolled from Beijing Youan Hospital (n = 435), Jiangxi Provincial People's Hospital (n = 50), Shijiazhuang Fifth Hospital (n = 36), and Hebei University Affiliated Hospital (n = 21). Inclusion criteria were: (1) patients with chronic HBV infection; (2) a single lesion ≤ 2 cm in diameter; (3) MRI with dynamic contrast

enhancement and DWI within 30 days before surgery; (4) confirmed pathological diagnosis; (5) no interventional therapy before MRI or surgery. Exclusion criteria: (1) non-HCC lesions such as hemangioma, hepatic cyst, or focal nodular hyperplasia; (2) Poorly differentiated HCC (Edmonson-Steiner grades III–IV); (3) poor MR image quality affecting assessment; (4) incomplete clinical, radiological, or pathological data; and (5) with other primary cancers or distant metastases. Ultimately, a total of 222 patients were enrolled in the study and randomly assigned to training and validation cohorts at a 7:3 ratio.[19] The patient selection process and cohort division are illustrated in Figure 1.

Collection of Clinical Data

Baseline patient data were collected from the electronic medical record system included gender, age, alpha-fetoprotein (AFP), AFP-L3%, white blood cell count (WBC), neutrophil count (NEU), lymphocyte count (LYM), platelet count (PLT), alanine aminotransferase (ALT), aspartate aminotransferase (AST), γ-glutamyl transferase (GGT), alkaline phosphatase (ALP), albumin (ALB), total bilirubin (TBIL), neutrophil-to-lymphocyte ratio (NLR), gamma-glutamyl transferase-to-lymphocyte ratio (GLR), aspartate aminotransferase-to-lymphocyte ratio (ALRI), and systemic immune-inflammation index (SII).

Pathologic Diagnosis

The pathological data were retrieved from the Pathology Information Management System, where diagnoses and grading were systematically recorded. Diagnostic criteria followed the 2019 WHO Classification of Tumours of the Digestive System. HCC histological grading was conducted using the modified Edmonson-Steiner system. Lesions ≤ 2 cm and classified as Grade I or II are defined as eHCC.

Image Acquisition

All patients underwent MRI using a 3.0T Siemens Magnetom Trio Tim scanner with a phased-array body coil covering the entire liver. Sequences included axial in-phase and out-of-phase T1-weighted imaging (FLASH), axial fat-suppressed T2-weighted imaging (SPAIR), diffusion-weighted imaging (DWI), and dynamic contrast-enhanced imaging with

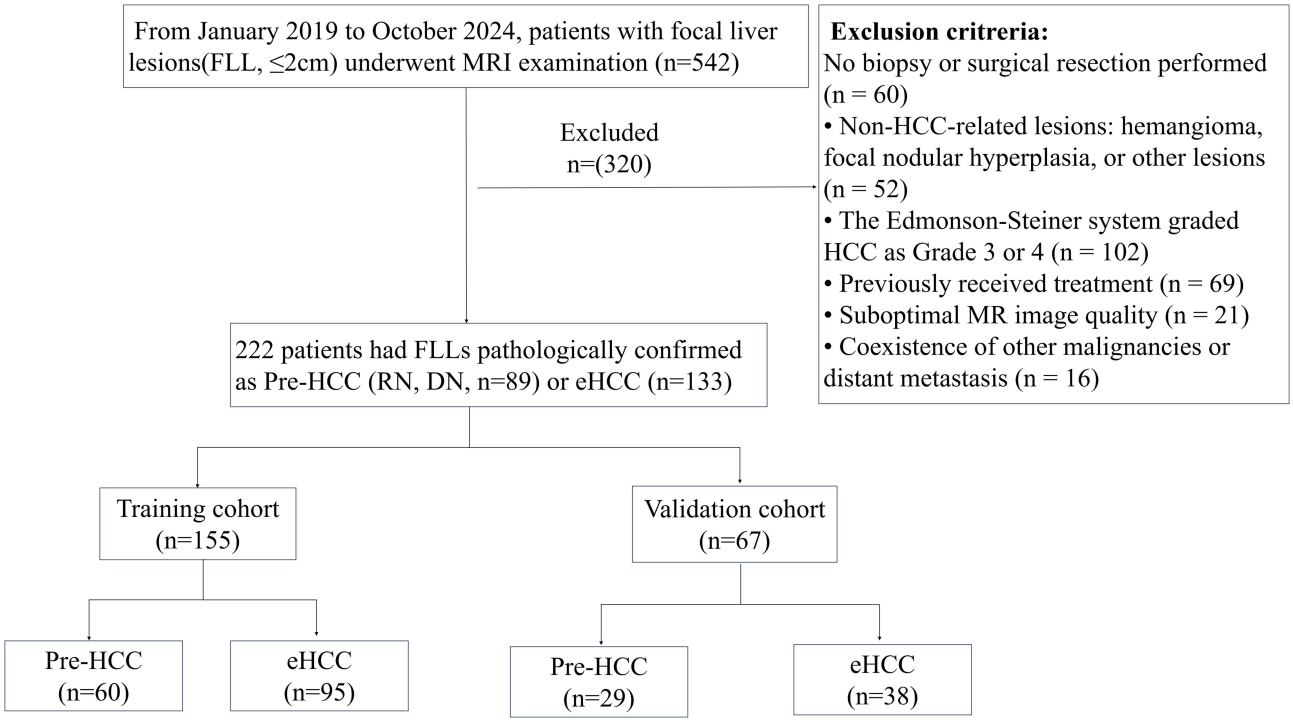

Figure 1 Patient selection flowchart.

https://doi.org/10.2147/JHC.S567418

a volumetric interpolated breath-hold (VIBE) sequence. Susceptibility-weighted imaging (SWI) was added for selected patients. Gadoxetic acid (Gd-EOB-DTPA; Primovist, Bayer Schering Pharma) was administered intravenously at 0.025 mmol/kg and 2.0 mL/s, followed by a 20 mL saline flush. Imaging phases were acquired at specific time points: arterial (17–19 s), late arterial/early portal (35–40 s), portal venous (60–80 s), equilibrium (180 s), and hepatobiliary (20 min) phases. All DWI sequences were acquired during free breathing using multiple signal averaging in combination with parallel imaging techniques to maximally suppress respiratory motion artifacts.

Qualitative Radiographic Analysis

Two board-certified radiologists with 18 and 20 years of experience in abdominal MRI independently evaluated the MRI features. They were unaware of the pathological results and clinical data. Discrepancies were resolved by consensus. The following imaging features were assessed: (1) T1-weighted imaging (T1WI) signal intensity; (2) T2-weighted imaging with fat suppression (T2WI-FS) signal intensity; (3) diffusion-weighted imaging (DWI) signal intensity; (4) enhancement pattern; and (5) presence of pseudocapsule.

Image Acquisition and Preprocessing

The radiomics workflow is shown in Figure 2. DICOM MRI images were obtained from the hospital's Picture Archiving and Communication System (PACS). Two experienced radiologists manually outlined three-dimensional regions of interest covering the entire tumor on consecutive cross-sectional images from the arterial phase (AP), portal venous phase (PVP), delayed phase (DP), and DWI using ITK-SNAP software. All images were preprocessed with voxel spacing resampled to $1\times1\times1$ mm^3 and intensity normalization applied to correct spatial variations and ensure gray-level consistency. To assess segmentation reliability, two radiologists independently re-segmented 30 randomly selected HCC cases one week after initial segmentation. Inter- and intra-observer agreement was evaluated using intraclass correlation coefficients (ICC), and only features with acceptable reproducibility (ICC > 0.75) were included in further analysis.

Feature Extraction and Selection

Peritumoral areas were defined by expanding the tumor ROI by 4 mm, 6 mm, and 8 mm using SimpleITK (encompass the most prevalent regions of microvascular invasion and microscopic satellite foci). When regions extend beyond the liver parenchyma, the operator manually adjusts the contour along the inner margin of the liver capsule or outer vascular

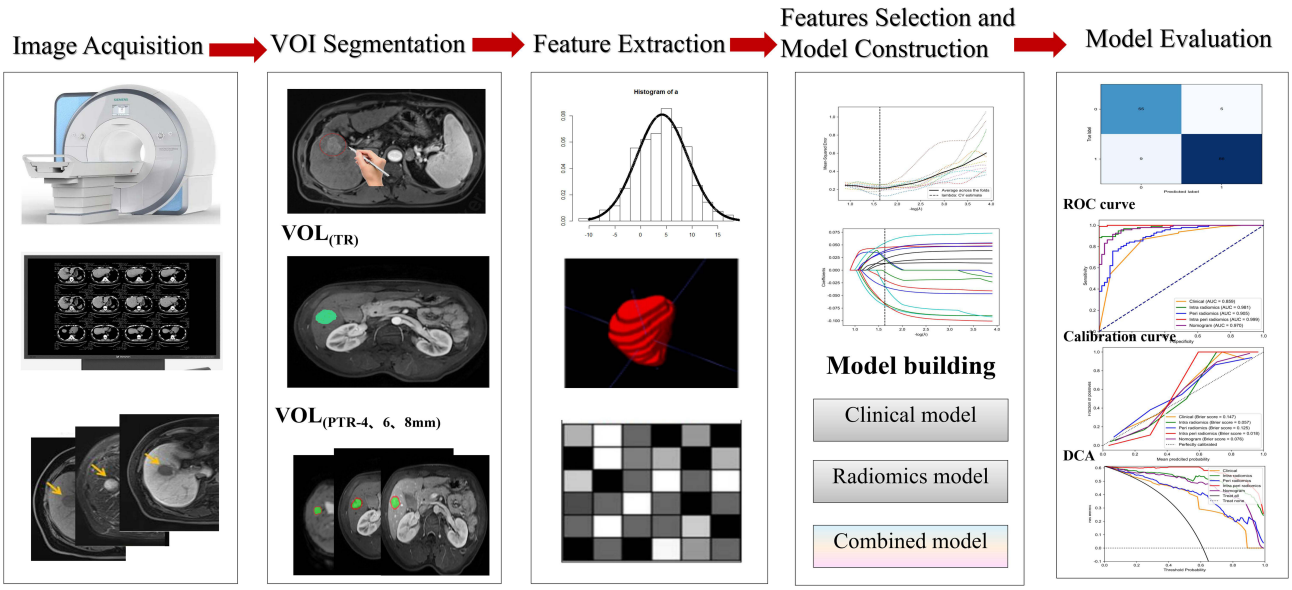

Figure 2 The flowchart illustrates the experimental workflow from MRI acquisition to ROI segmentation, peritumoral dilation, feature selection, model construction, and final evaluation. In the schematic images, arrows denote the manually segmented intratumoral ROI, whereas the highlighted contours indicate the peritumoral regions generated by fixed-distance expansion.

boundary to ensure the segmented area remains within functional hepatic parenchyma. All adjustments use axial images from the arterial or portal venous phases, reference all available sequences, and are reviewed by a second investigator. Radiomics features were extracted using PyRadiomics (version 3.6.0), including first-order statistics, shape-based features, and texture features derived from multiple matrices—namely, the gray-level co-occurrence matrix (GLCM), gray-level size zone matrix (GLSZM), gray-level run length matrix (GLRLM), neighborhood gray-tone difference matrix (NGTDM), and gray-level dependence matrix (GLDM). Extraction was performed across all MRI sequences and spatial regions, resulting in 1409 features per patient after z-score standardization. A three-step feature selection process was then applied to identify optimal radiomic features. First, variance thresholding removed low-variance features (threshold = 0.8). Second, univariate analysis selected features significantly associated with the outcome ($p < 0.05$). Finally, LASSO regression with ten-fold cross-validation identified the optimal subset using regularization parameters.

Model Development

Logistic regression models were constructed to distinguish early HCC from precancerous lesions. Individual models were developed for intratumoral features and each peritumoral region (Peri_4mm, Peri_6mm, Peri_8mm). The optimal peritumoral model was selected based on prediction performance, and its features were subsequently combined with intratumoral features to create the final IntraPeri fusion model. A comprehensive nomogram model was then developed by integrating the clinical predictors with the IntraPeri radiomics signatures to enhance diagnostic performance.

Model Stability Assessment

Model stability was assessed via ten-fold cross-validation performed on the training cohort. To further evaluate internal validity, bootstrap validation with 1,000 resampling iterations was conducted on the full cohort to estimate optimism-corrected performance metrics.

Statistical Analysis

Statistical analysis was conducted using SPSS 27.0 (IBM, Armonk, NY, USA), R (v4.2.1), and Python (v3.6.12). Normally distributed data are presented as mean ± SD; otherwise, median (IQR) is reported. Continuous variables were compared with the Student's *t*-test or Mann–Whitney *U*-test based on distribution. Categorical variables were analyzed using the chi-square or Fisher's exact test, as appropriate. Variables with $p < 0.05$ in univariate logistic regression were included in multivariate analysis to identify independent predictors. Differences in AUC between models in the testing set were evaluated using the DeLong test. Model calibration and clinical applicability were assessed with calibration curves and decision curve analysis. All *p*-values were two-sided, with significance set at $p < 0.05$.

Results

Baseline Characteristics

This study enrolled 222 patients with pathologically confirmed liver nodules. Of these, 133 were diagnosed with eHCC, and 89 had pre-HCC lesions, including 42 with LGDN and 47 with HGDN. Among the participants, 164 were male (73.9%), with a mean age of 57.2 ± 11.0 years (range: 21–86). All patients were randomly assigned to a training cohort [n = 155; 96 eHCC (60.26%), 59 pre-HCC (39.74%)] and a validation cohort [n = 67; 37 eHCC (59.09%), 30 pre-HCC (40.91%)]. Clinical and MRI features of both cohorts are summarized in Table 1, with no significant differences in baseline characteristics between the groups.

Clinical Risk Features and Model Development

Univariate logistic analysis showed that T1WI signal intensity, T2WI signal intensity, DWI, enhancement pattern, WBC, LYM, PLT, GLR, and ALRI were significantly associated with eHCC in the training cohort (all $p < 0.05$). Multivariate analysis further identified T1WI signal intensity, DWI, and GLR as independent predictors of eHCC (Table 2). A clinical model incorporating these three independent variables demonstrated strong discriminative performance, with AUC values of 0.826 (95% CI: 0.754–0.899) in the training cohort and 0.795 (95% CI: 0.683–0.908) in the validation cohort.

Table 1 Baseline Characteristics of Patients with Pre-HCC and eHCC in the Training and Validation Cohorts

Variables	Training Cohort (n=155)			Validation Cohort (n=67)			*p* Value
	Pre-HCC (n = 59)	eHCC (n = 96)	*p* Value	Pre-HCC (n = 30)	eHCC (n = 37)	*p* Value	
Age, Mean ± SD	56.1 ± 10.6	58.8 ± 10.3	0.118	52.4±12.9	58.7 ±10.6	0.044	0.181
Gender, n (%)			0.258			0.398	0.245
Female	17 (28.8)	20 (20.8)		11 (36.7)	10 (27.0)		
Male	42 (71.2)	76 (79.2)		19 (63.3)	27 (73.0)		
Tumor markers							
AFP, μg/L	6.5 (3.1, 54.2)	6.6 (2.3, 40.4)	0.580	5.2 (2.5, 30.2)	12.8(4.4, 54.7)	0.097	0.645
AFP-L3>10%, n (%)	7 (11.9)	15 (15.6)	0.515	6 (20.0)	8 (21.6)	0.871	0.214
Blood routine test							
WBC, $\times10^9$/L, Mean ± SD	4.5±2.2	5.1±2.1	0.027	4.2±2.7	5.1±2.0	0.02	0.459
NEU, $\times10^9$/L	2.2 (1.2, 3.4)	2.7 (2.0, 3.4)	0.106	1.9 (1.3, 3.0)	2.8 (2.0, 4.0)	0.026	0.812
LYM, $\times10^9$/L	1.2 (0.7, 1.9)	1.5 (1.0, 1.9)	0.020	1.2 (0.8, 2)	1.4 (0.9, 1.9)	0.152	0.088
PLT, $\times10^9$/L, Mean ± SD	109.4±55.6	128.9 ±50.9	0.010	87.8±53.2	124.5±71)	0.019	0.049
Liver function test							
ALT, U/mL	26.8 (20.0, 40.0)	27.1(20.0, 45.0)	0.828	27.5 (22.0, 40.0)	29.0 (19.7, 52.6)	0.724	0.604
AST, U/mL	33.3 (25.0, 42.0)	29.0 (23.0, 44.0)	0.246	36.4 (30.8, 52.0)	29.0 (22.0, 48.0)	0.063	0.270
GGT, U/L	46.0 (30.0, 61.6)	33.8 (23.0, 72.9)	0.068	46.0 (28.0, 58.0)	38.0 (26.0, 55.7)	0.570	0.956
ALP, U/L	83.0 (68.0, 107.0)	79.0 (65.2, 99.0)	0.378	90.0 (74.0, 137.5)	77.0 (61.1, 97.5)	0.011	0.512
ALB, g/L	37.7 (34.4, 43.2)	40.9 (37.4, 43.5)	0.068	34.5 (31.5, 40.4)	41.6 (37.7, 43.7)	0.008	0.259
TB, umol/L, Mean ± SD	21.9±11.8	21.1±9.7	0.874	28.1±16.8	22.9±12.4	0.145	0.635
Inflammatory-related parameters							
NLR	2.0 (1.3, 3.0)	1.8 (1.3, 2.5)	0.410	1.8 (1.0, 2.9)	2.1 (1.7, 3.0)	0.164	0.283
GLR	47.8 (18.3, 85.1)	27.8 (15.8, 45.7)	0.005	42.7 (26.3, 73.2)	31.2 (23.2, 47.8)	0.019	0.160
SII	185.6 (92.6, 347.1)	239.5 (142.4, 376.7)	0.117	131.4 (73.4, 254.4)	262.5 (135.3, 437.0)	0.013	0.51
ALRI	29.8 (17.3, 65.3)	20.0 (14.3, 39.1)	0.018	42.8 (21.6, 76.0)	29.7 (13.6, 38.0)	0.038	0.094
Imaging features							
T1WIn (%)			< 0.001			0.004	0.059
Hypointense	30 (50.8)	89 (92.7)		14 (46.7)	30 (81.1)		
Isointense	4 (6.8)	1 (1.0)		4 (13.3)	4 (10.8)		
Hyperintense	25 (42.4)	6 (6.3)		12 (40.0)	3 (8.1)		
T2WI.fs, n (%)			< 0.001			0.041	0.369
Hypointense	11 (18.6)	1 (1.0)		6 (20.0)	1 (2.7)		
Isointense	14 (23.7)	7 (7.3)		7 (23.3)	7 (18.9)		
Hyperintense	34 (57.6)	88 (91.7)		17 (56.7)	29 (78.4)		
DWI, n (%)			< 0.001			0.011	0.814
Hypointense	4 (6.8)	1 (1.0)		2 (6.7)	1 (2.7)		
Isointense	27(45.8)	5 (5.2)		13 (43.3)	5 (13.5)		
Hyperintense	28 (47.5)	90 (93.8)		15 (50.0)	31 (83.8)		
Enhancement pattern, n (%)			0.001			0.033	0.371
None	11 (18.6)	1 (1.0)		6 (20.0)	2 (5.4)		
Homogeneous	22 (37.3)	34 (35.4)		11 (36.7)	8 (21.6)		
Heterogeneous	26 (44.1)	61 (69.6)		13 (43.3)	27 (73.0)		
Pseudocapsule, n (%)			0.004			0.029	0.394
Absent	47 (79.7)	55 (57.3)		26 (86.7)	22 (59.5)		
Present	12 (20.3)	41(42.7)		4 (13.3)	15 (40.5)		

Performance Evaluation and Comparison of the Models

The features demonstrated excellent reproducibility (mean ICC = 0.94; Table S1). The feature selection process for each VOI and imaging sequence is detailed in Table S2. The intratumoral model achieved AUC values of 0.871 (95% CI: 0.814–0.928) in the training cohort and 0.860 (95% CI: 0.769–0.952) in the validation cohort. Among the three peritumoral models, Peri_6mm showed the highest performance, with AUCs of 0.879 (95% CI: 0.828–0.931) and 0.831 (95% CI: 0.728–0.933) in the training and validation cohorts, respectively. The Peri_8mm model followed closely

Table 2 Univariate and Multivariate Analysis for eHCC Prediction

Characteristics	Univariate			Multivariate		
	OR	95% CI	*p*-Value	OR	95% CI	*p*-Value
T1WI			<0.001			0.034
T1WI (Middle vs Low)	0.455	0.112–1.766	0.250			
T1WI (High vs Low)	0.059	0.019–0.185	<0.001	0.187	0.052–0.675	0.011
T2WI			<0.001			
T2WIfs (Middle vs Low)	5.500	0.586–51.620	0.136			
T2WIfs (High vs Low)	28.471	3.539–229.039	0.002			
DWI			<0.001			<0.001
DWI (Middle vs Low)	0.700	0.116–4.232	0.698			
DWI (High vs Low)	11.348	2.147–59.979	0.004	8.134	1.330–49.743	0.023
Enhancement			0.008			
Enhancement (Homogeneous vs None)	17.000	2.048–141.091	0.009			
Enhancement (Heterogeneous vs None)	25.808	3.167–210.319	0.002			
Pseudocapsule (Present)	3.825	1.631–8.696	0.002			
WBC	1.153	0.972–1.368	0.102			
Lymphocyte	1.626	0.992–2.665	0.054			
PLT	1.008	1.002–1.015	0.012			
GLR	0.988	0.981–0.996	0.004	0.989	0.980–0.999	0.026
ALRI	1.000	0.997–1.004	0.902			

(AUCs: 0.866 and 0.830), as did the Peri_4mm model (AUCs: 0.820 and 0.760). Notably, combining features from the intratumoral and Peri_6mm regions into the IntraPeri model significantly improved predictive performance, yielding AUCs of 0.947 (95% CI: 0.916–0.978) and 0.935 (95% CI: 0.877–0.993) in the training and validation cohorts, respectively (Figure 3, Supplementary Figures 1, 2 and Table S3).

A nomogram model was developed by integrating three clinical features with the IntraPeri radiomics model (Figure 4). It showed AUCs of 0.958 (95% CI: 0.928–0.987) in the training cohort and 0.950 (95% CI: 0.900–0.999) in the validation cohort. Notably, in the validation set, the nomogram model achieved the highest positive predictive value (PPV), whereas the IntraPeri radiomics model demonstrated the highest negative predictive value (NPV) (Table 3). The classification performance of the IntraPeri model and the nomogram in the validation cohort is further illustrated by the corresponding confusion matrices (Supplementary Figure 3). DeLong tests in the validation cohort revealed significant differences

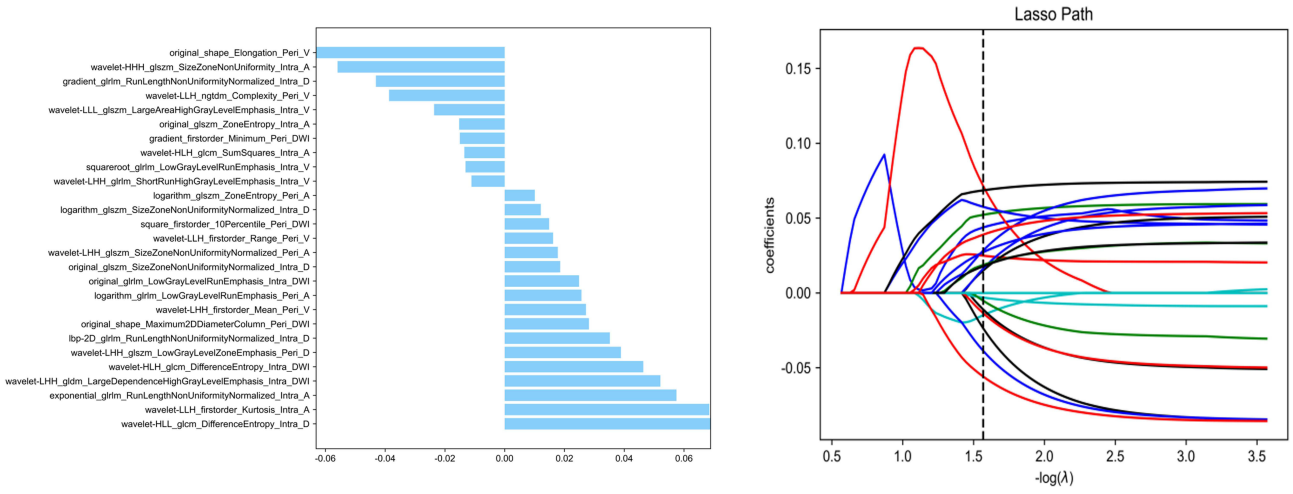

Figure 3 Weighted importance of the 27 selected features based on the LASSO method in the IntraPeri fusion model.

https://doi.org/10.2147/JHC.S567418

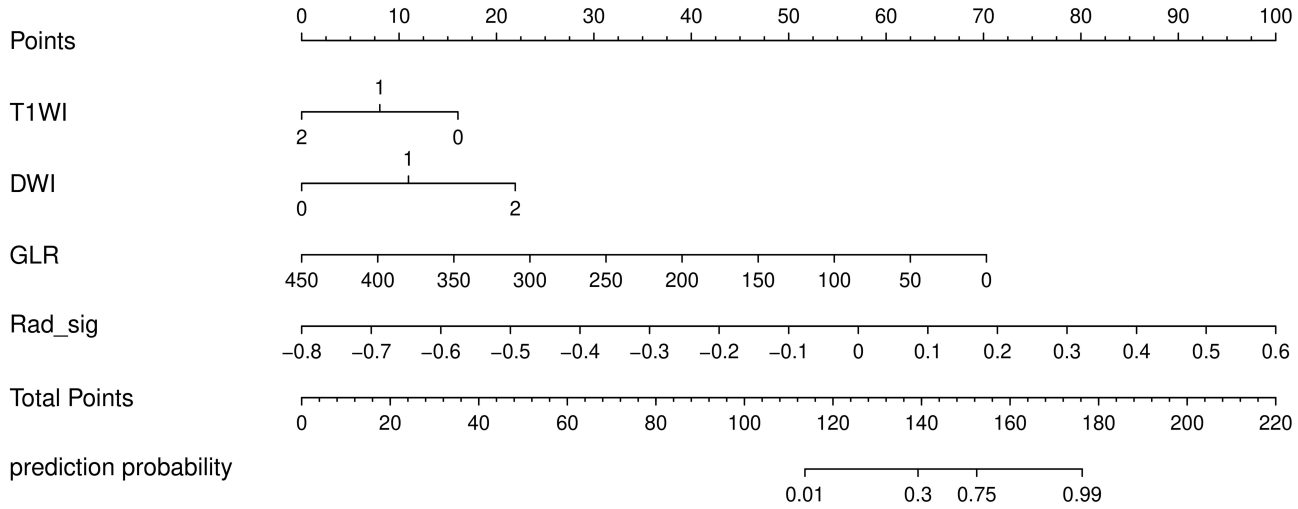

Figure 4 Clinical-radiomics nomogram for predicting early hepatocellular carcinoma (eHCC). The nomogram integrates clinical variables (T1WI, DWI, GLR) and the radiomics score (Rad_sig) to predict the probability of early hepatocellular carcinoma. Each variable corresponds to a specific point on the "Points" scale, which reflects its relative contribution (weight) in the final model. By summing the total points and projecting them onto the "Prediction Probability" scale, the individual risk of eHCC can be estimated.

between the nomogram and both the clinical ($p = 0.001$) and intratumoral models ($p = 0.013$), while showing no significant difference compared to the IntraPeri model ($p = 0.266$) (Table S4). Decision curve analysis and calibration plots (Figure 5) confirmed its higher net benefit and reliability in distinguishing eHCC from precancerous nodules.

Model Interpretation

To explore the nomogram model's decision-making mechanism, SHAP was used for interpretability analysis. Results showed that the radiomics signature combining intratumoral and peritumoral regions (Rad_sig) had the highest feature importance, followed by DWI, T1WI, and GLR. T1WI hypointensity and low GLR values were associated with a higher likelihood of eHCC, while elevated Rad_sig and DWI hyperintensity positively contributed to eHCC diagnosis. The model's reasoning is illustrated in Figure 6.

Discussion

Our study developed an integrated predictive model combining clinical variables and radiomic features from intratumoral and peritumoral regions on multiparametric MRI. The intratumoral model showed a validation AUC of 0.838, demonstrating effective diagnostic performance. The fusion model combined intratumoral and optimal peritumoral features, showing better performance than the intratumoral-only model in both training and validation cohorts, which highlights the value of peritumoral radiomics. Integrating clinical variables into a nomogram further improved predictive performance, indicating that these variables complement radiomic signatures to enhance diagnostic accuracy.

Our study confirmed that T1WI hypointensity and DWI hyperintensity serve as independent predictors for differentiating eHCC from precancerous nodules. T1WI hypointensity reflects changes in cellular composition and microenvironmental remodeling, indicating a progressive transition from precancerous to malignant lesions.[20] Gao et al[21] found that T1WI hypointensity was significantly associated with eHCC, consistent with the findings of this study. DWI hyperintensity reflects increased cellularity and reduced extracellular space, which are hallmarks of early malignant transformation. The combination of contrast-enhanced MRI and DWI has been shown to enhance the detection rate of primary HCC and improve the accuracy of hepatic pathology classification, offering superior diagnostic performance.[22,23] Furthermore, combining T1WI and DWI signal patterns improves diagnostic accuracy for small HCCs, consistent with the findings of this study.[10] In this study, the clinical model incorporating these imaging features achieved moderate diagnostic performance (AUC: 0.795), supporting their utility as fundamental imaging biomarkers.

This study identified GLR as an independent predictor of eHCC. Contrary to previous reports linking elevated GLR to poor HCC prognosis, our findings show reduced GLR in eHCC compared to precancerous nodules. This discrepancy

Table 3 Performance Details of the Different Model for Predicting eHCC

Model Name	Number of Features		AUC (95% CI)	Accuracy	Sensitivity	Specificity	PPV	NPV
Clinical	3	Training	0.826 (0.754–0.899)	0.787	0.823	0.729	0.824	0.727
		Validation	0.795 (0.683–0.908)	0.761	0.757	0.767	0.800	0.719
Intratumoral radiomics	30	Training	0.884(0.830–0.939)	0.813	0.854	0.746	0.854	0.746
		Validation	0.838(0.743–0.933)	0.731	0.811	0.633	0.732	0.731
Peritumoral_4 radiomics	20	Training	0.820(0.753–0.886)	0.729	0.708	0.763	0.825	0.628
		Validation	0.760(0.644–0.877)	0.687	0.649	0.733	0.750	0.629
Peritumoral_6 radiomics	35	Training	0.879(0.828–0.931)	0.768	0.781	0.746	0.837	0.673
		Validation	0.831(0.728–0.933)	0.776	0.811	0.733	0.789	0.759
Peritumoral_8 radiomics	35	Training	0.866(0.808–0.925)	0.774	0.823	0.695	0.806	0.718
		Validation	0.830(0.731–0.929)	0.776	0.892	0.633	0.750	0.826
Intraperi radiomics	27	Training	0.947 (0.916–0.978)	0.877	0.865	0.898	0.947	0.773
		Validation	0.935 (0.877–0.993)	0.881	0.919	0.833	0.872	0.893
Combined nomogram	4	Training	0.958(0.928–0.987)	0.903	0.917	0.881	0.934	0.854
		Validation	0.950 (0.900–0.999)	0.896	0.865	0.933	0.941	0.849

https://doi.org/10.2147/JHC.S567418

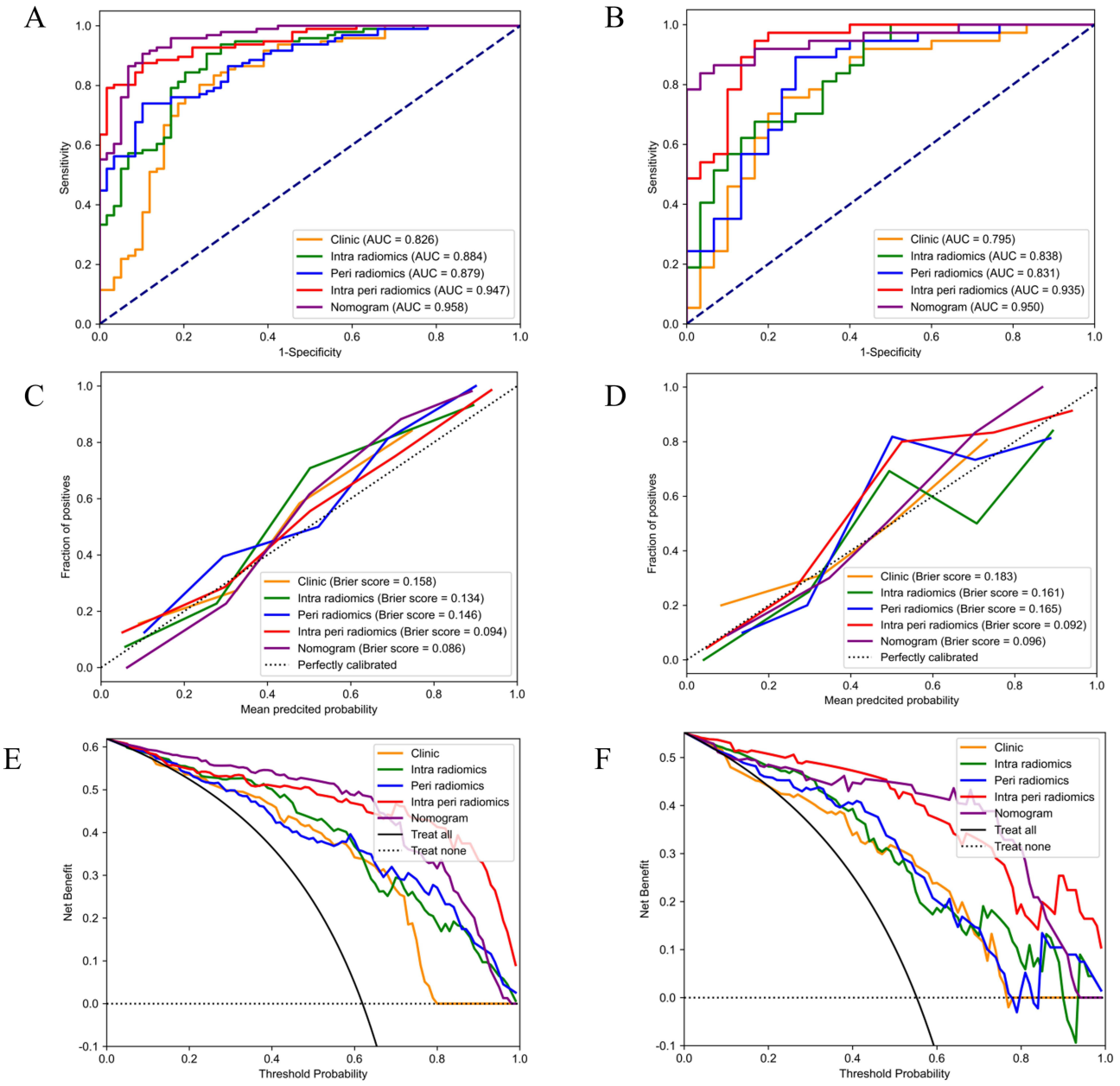

Figure 5 Model performance evaluation for predicting early hepatocellular carcinoma (eHCC). (**A** and **B**) ROC curves comparing clinical, intratumoral radiomics, peritumoral radiomics, IntraPeri, and combined nomogram models in the training (**A**) and validation (**B**) cohorts. (**C** and **D**) Calibration curves assessing prediction accuracy in the training (**C**) and validation (**D**) cohorts. (**E** and **F**) Decision curve analysis evaluating clinical utility across different threshold probabilities in the training (**E**) and validation (**F**) cohorts.

may be attributed to the inclusion of eHCC cases, where the host immune system has not yet mounted a strong anti-tumor response.[24,25] The relatively elevated GLR in precancerous lesions may represent an initial immune-mediated reaction to early neoplastic changes, suggesting GLR could serve as a biomarker for immune status assessment in early liver carcinogenesis. Nonetheless, large-scale, multi-center studies are needed to validate these findings and evaluate the generalizability of GLR across diverse patient populations.

Radiomics analysis enabled extraction of quantitative texture features that correlated with underlying pathological characteristics, overcoming limitations of conventional visual interpretation.[26] It has shown robust performance in differentiating benign from malignant liver lesions,[27,28] predicting histological grades of HCC,[29] and staging liver fibrosis.[30] Zhong et al[15] developed a model based on T1WI, T2WI, and apparent diffusion coefficient (ADC) MRI

 https://doi.org/10.2147/JHC.S567418

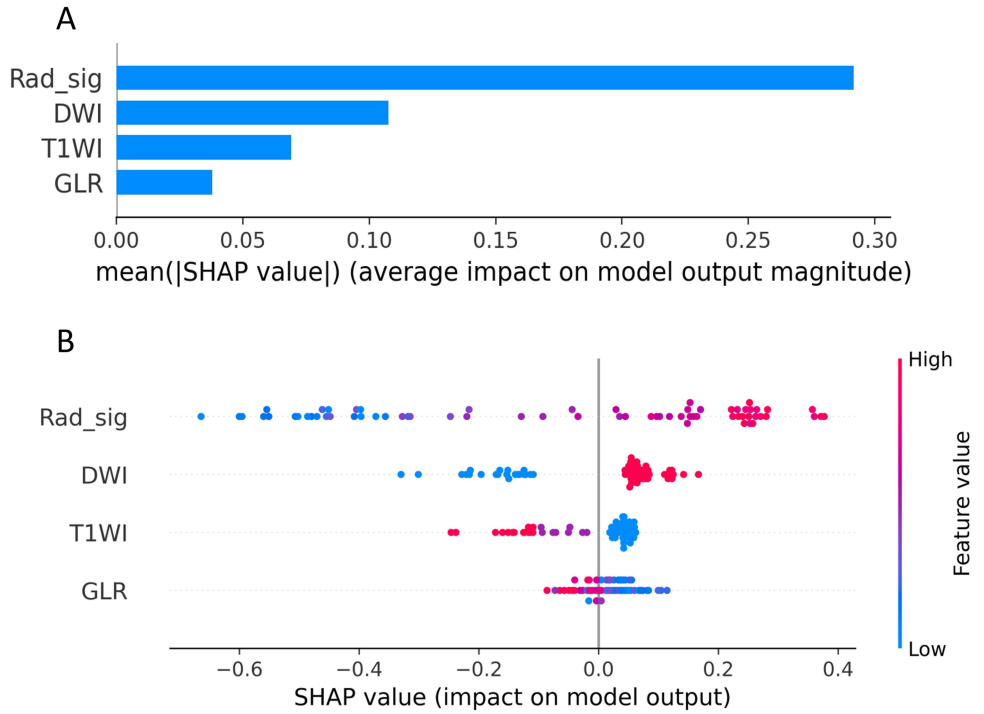

Figure 6 SHAP analysis for model interpretability. The bar plot (**A**) displays the ranking of feature importance, while the beeswarm plot (**B**) illustrates the positive and negative contributions of each variable in individual predictions.

images to distinguish small HCC from benign nodules, achieving an AUC of 0.917; integration with LI-RADS v2018 increased the AUC to 0.975. Gao et al[21] developed a model using non-enhanced MRI sequences, in which the T1+FS-T2 combination achieved optimal performance (AUC = 0.95), significantly outperforming radiologists' diagnostic accuracy (AUC = 0.518). Sun et al[31] constructed a multi-phase MRI-based model to identify micro-premalignant lesions, achieving intra-group and inter-group AUCs of 0.93 and 0.97, with test cohort accuracies of 86.67% and 94.12%, respectively. These studies collectively demonstrate the strong potential of MRI-based radiomics for early HCC diagnosis. In this study, a systematic feature selection pipeline was employed to effectively reduce dimensionality while preserving stable and representative features. The intratumoral radiomics model demonstrated satisfactory diagnostic performance (AUC: 0.860), consistent with findings from previous studies,[11,21] further reinforcing the clinical applicability of MRI-based radiomics in the early detection of HCC.

Peritumoral tissues can provide valuable pathological insights into HCC.[32] In the field of radiomics research, the inclusion of this region represents a transition from a solely tumor-centric evaluation to a more comprehensive analysis of the tumor microenvironment. Liu et al[19] developed an IntraPeri fusion model using multiparametric MRI to predict HCC histological differentiation, achieving AUCs of 0.95 and 0.86 in the training and validation cohorts, respectively—both higher than those of the intratumoral-only model (AUCs: 0.92 and 0.82) and individual peritumoral models. Similarly, Zhao et al[33] demonstrated in their study on transarterial chemoembolization response prediction that the fusion model outperformed models utilizing only intratumoral or only peritumoral features. These findings demonstrate that peritumoral textures are essential for understanding tumor microenvironment dynamics and invasiveness, and incorporating this information can significantly enhance diagnostic accuracy.[34,35] Discrepancies in patient characteristics, study objectives, and tumor size have led to variations in the optimal peritumoral boundary widths reported across HCC studies. Wang et al[36] reported that a 5 mm margin beyond the tumor provided the best predictive performance, whereas Liu et al[19] and Chong et al[37] independently demonstrated superior diagnostic accuracy with a 10 mm boundary. In this study, three peritumoral models—Peri_4mm, Peri_6mm, and Peri_8mm—were developed to assess their ability to differentiate eHCC from precancerous nodules. All models showed varying discriminative performance, with AUC values of 0.730, 0.805, and 0.788, respectively, and the Peri_6mm model achieved the highest performance. Evidence indicates that overly narrow boundary definitions may fail to capture significant

https://doi.org/10.2147/JHC.S567418

histopathological changes in adjacent tissues, while excessively wide boundaries may include nonspecific anatomical structures—such as major vessels or bile ducts—introducing heterogeneity-related noise and reducing model reliability.[16] In this study, the 6 mm boundary appears to represent an optimal compromise, effectively capturing biologically meaningful alterations while minimizing interference from irrelevant anatomical components. Nonetheless, there is consensus that precise boundary delineation is essential for effective peritumoral modeling.

The Peri_6mm model was combined with the intratumoral model to form the IntraPeri fusion model, which demonstrated superior predictive performance (AUC: 0.921 vs 0.860). This confirms prior findings and indicates that peritumoral tissue provides valuable insights into tumor biology and heterogeneity when integrated with intratumoral data.[17] The nomogram model developed in this study demonstrated superior diagnostic performance (AUC = 0.950) and greater clinical net benefit. Although no significant difference was found between this model and the IntraPeri model, the result indirectly indicates that the IntraPeri approach has diagnostic potential. It also shows that clinical features positively enhance AUC and decision curve performance. Compared with the traditional intratumoral-based radiomics model, our integrated approach may provide better accuracy and stability in distinguishing eHCC from precancerous nodules. While the current model exhibits markedly superior performance relative to conventional serological biomarkers—such as alpha-fetoprotein (AFP) and protein induced by vitamin K antagonist-II (PIVKA-II)—in detecting eHCC,[38,39] several challenges must still be overcome before its integration into routine clinical practice. Key requirements include robust external validation, the development of user-friendly software platforms, and comprehensive training programs for healthcare professionals in the interpretation and application of radiomics data.[16]

Limitations

This study has several limitations. First, its retrospective design makes it prone to selection bias, which may affect the generalizability and external validity of the results. Second, the inclusion criteria limited the analysis to lesions ≤ 2 cm in diameter, resulting in a small sample size that may reduce the statistical power and robustness of the predictive models. Third, not all patients underwent MRI with Gd-EOB-DTPA contrast-enhanced hepatobiliary phase imaging, limiting the analysis of radiomic features specific to this phase. Fourth, the peritumoral region was defined using a fixed-distance expansion method, which may fail to capture the biological heterogeneity across tumors of different sizes. Finally, some patients had insufficient follow-up to assess the model's long-term prognostic value.

Conclusion

The fusion model combining intratumoral and peritumoral MRI radiomic features outperforms conventional single-region methods in detecting HBV-related eHCC. Notably, the 6 mm peritumoral boundary provides new diagnostic insights into eHCC characterization. The nomogram model shows the highest predictive accuracy and clinical utility, offering a promising non-invasive approach for early eHCC detection and evidence-based clinical decisions.

Data Sharing Statement

The original contributions presented in the study are included in the article/Supplementary Material. Further inquiries can be directed to the corresponding author.

Ethics Statement

This study was conducted in strict accordance with the ethical principles outlined in the Declaration of Helsinki. Approval was granted by the Ethics Committee of Beijing Youan Hospital, Capital Medical University. In consideration of the anonymized nature of the data and the non-interventional study design, the requirement for written informed consent was waived in compliance with applicable regulatory guidelines.

Author Contributions

All authors made a significant contribution to the work reported, whether that is in the conception, study design, execution, acquisition of data, analysis and interpretation, or in all these areas; took part in drafting, revising or critically reviewing the article; gave final approval of the version to be published; have agreed on the journal to which the article has been submitted; and agree to be accountable for all aspects of the work.

Funding

The authors declare that no financial support was received for the research and/or publication of this article.

Disclosure

The authors declare that the research was conducted in the absence of any commercial or financial relationships that could be construed as a potential conflict of interest.

References

1. Bray F, Laversanne M, Sung H. et al. Global cancer statistics 2022: GLOBOCAN estimates of incidence and mortality worldwide for 36 cancers in 185 countries. *CA Cancer J Clin*. 2024;74(3):229–263. doi:10.3322/caac.21834
2. Yan R, Sun M, Yang H, Du S, Sun L, Mao Y. 2024 latest report on hepatitis B virus epidemiology in China: current status, changing trajectory, and challenges. *Hepatobiliary Surg Nutr*. 2025;14(1):66–77. doi:10.21037/hbsn-2024-754
3. Rhee H, Park YN, Choi JY. Advances in understanding hepatocellular carcinoma vasculature: implications for diagnosis, prognostication, and treatment. *Korean J Radiol*. 2024;25(10):887–901. doi:10.3348/kjr.2024.0307
4. International Consensus Group for Hepatocellular Neoplasia. Pathologic diagnosis of early hepatocellular carcinoma: a report of the international consensus group for hepatocellular neoplasia. *Hepatology*. 2009;49:658–664. doi:10.1002/hep.22709
5. Nagtegaal ID, Odze RD, Klimstra D, et al. The 2019 WHO classification of tumours of the digestive system. *Histopathology*. 2020;76:182–188. doi:10.1111/his.13975
6. Yokoo T, Masaki N, Parikh ND, et al. Multicenter validation of abbreviated MRI for detecting early-stage hepatocellular carcinoma. *Radiology*. 2023;307:e220917. doi:10.1148/radiol.220917
7. Wu ST, Zhu L, Feng XL, Wang HY, Li F. Strategies for discovering novel hepatocellular carcinoma biomarkers. *World J Hepatol*. 2025;17:101201. doi:10.4254/wjh.v17.i2.101201
8. Hytiroglou P. Well-differentiated hepatocellular nodule: making a diagnosis on biopsy and resection specimens of patients with advanced stage chronic liver disease. *Semin Diagn Pathol*. 2017;34:138–145. doi:10.1053/j.semdp.2016.12.009
9. Lee YJ, Lee JM, Lee JS, et al. Hepatocellular carcinoma: diagnostic performance of multidetector CT and MR imaging—a systematic review and meta-analysis. *Radiology*. 2015;275(1):97–109. doi:10.1148/radiol.14140690
10. Renzulli M, Giampalma E. Hepatocellular carcinoma: imaging advances in 2024 with a focus on magnetic resonance imaging. *Curr Oncol*. 2025;32(1):40. doi:10.3390/curroncol32010040
11. Park MJ, Kim YK, Lee MH, Lee JH. Validation of diagnostic criteria using gadoxetic acid-enhanced and diffusion-weighted MR imaging for small hepatocellular carcinoma (≤2.0 cm) in patients with hepatitis-induced liver cirrhosis. *Acta Radiol*. 2013;54(2):127–136. doi:10.1258/ar.2012.120262
12. Renzulli M, Biselli M, Brocchi S, et al. New hallmark of hepatocellular carcinoma, early hepatocellular carcinoma and high-grade dysplastic nodules on Gd-EOB-DTPA MRI in patients with cirrhosis: a new diagnostic algorithm. *Gut*. 2018;67(9):1674–1682. doi:10.1136/gutjnl-2017-315384
13. Lin B, Zhang W, Jiang Y, et al. Diagnostic performance of LR-5 based on hypointensity on Gd-EOB-DTPA-enhanced MRI in the hepatobiliary phase for sHCC using LI-RADS v2018 criteria. *Clin Radiol*. 2025;81:106784. doi:10.1016/j.crad.2024.106784
14. Brancato V, Cerrone M, Garbino N, Salvatore M, Cavaliere C. Current status of magnetic resonance imaging radiomics in hepatocellular carcinoma: a quantitative review with Radiomics Quality Score. *World J Gastroenterol*. 2024;30(4):381–417. doi:10.3748/wjg.v30.i4.381
15. Zhong X, Guan T, Tang D, et al. Differentiation of small (≤3 cm) hepatocellular carcinomas from benign nodules in cirrhotic liver: the additive value of MRI-based radiomics analysis to LI-RADS version 2018 algorithm. *BMC Gastroenterol*. 2021;21(1):155. doi:10.1186/s12876-021-01710-y
16. Huang Y, Qian H. Advancing hepatocellular carcinoma management through peritumoral radiomics: enhancing diagnosis, treatment, and prognosis. *J Hepatocell Carcinoma*. 2024;11:2159–2168. doi:10.2147/JHC.S493227
17. Qian H, Huang Y, Xu L, Fu H, Lu B. Role of peritumoral tissue analysis in predicting characteristics of hepatocellular carcinoma using ultrasound-based radiomics. *Sci Rep*. 2024;14(1):11538. doi:10.1038/s41598-024-62457-6
18. Chong HH, Yang L, Sheng RF, et al. Multi-scale and multi-parametric radiomics of gadoxetate disodium-enhanced MRI predicts microvascular invasion and outcome in patients with solitary hepatocellular carcinoma ≤5 cm. *Eur Radiol*. 2021;31(7):4824–4838. doi:10.1007/s00330-020-07601-2
19. Liu HF, Wang M, Wang Q, et al. Multiparametric MRI-based intratumoral and peritumoral radiomics for predicting the pathological differentiation of hepatocellular carcinoma. *Insights Imaging*. 2024;15(1):97. doi:10.1186/s13244-024-01623-w
20. Chou CT, Chou JM, Chang TA, et al. Differentiation between dysplastic nodule and early-stage hepatocellular carcinoma: the utility of conventional MR imaging. *World J Gastroenterol*. 2013;19(42):7433–7439. doi:10.3748/wjg.v19.i42.7433
21. Gao X, Bian J, Luo J, et al. Radiomics-based distinction of small (≤2 cm) hepatocellular carcinoma and precancerous lesions based on unenhanced MRI. *Clin Radiol*. 2024;79(5):e659–e664. doi:10.1016/j.crad.2024.01.019
22. Scialpi M, Evangelisti A, Shehu K, Comite P, Antogiovanni GN, Scalera GB. Standardizing diffusion-weighted imaging in LI-RADS for diagnosis of hepatocellular carcinoma. *Eur Radiol*. 2025;35(2):695–697. doi:10.1007/s00330-024-10925-y
23. Surov A, Pech M, Omari J, et al. Diffusion-weighted imaging reflects tumor grading and microvascular invasion in hepatocellular carcinoma. *Liver Cancer*. 2021;10(1):10–24. doi:10.1159/000511384
24. Wang Y, Zhou CW, Zhu GQ, et al. A multidimensional nomogram combining imaging features and clinical factors to predict the invasiveness and metastasis of combined hepatocellular cholangiocarcinoma. *Ann Transl Med*. 2021;9(20):1518. doi:10.21037/atm-21-2500
25. Zhou PC, Huang R, Wang HT, et al. Gamma-glutamyl transferase-to-lymphocyte ratio as a prognostic marker in patients with hepatocellular carcinoma undergoing hepatectomy. *World J Gastrointest Surg*. 2025;17(2):98578. doi:10.4240/wjgs.v17.i2.98578
26. Lambin P, Leijenaar RTH, Deist TM, et al. Radiomics: the bridge between medical imaging and personalized medicine. *Nat Rev Clin Oncol*. 2017;14(12):749–762. doi:10.1038/nrclinonc.2017.141
27. Wu J, Liu A, Cui J, Chen A, Song Q, Xie L. Radiomics-based classification of hepatocellular carcinoma and hepatic haemangioma on precontrast magnetic resonance images. *BMC Med Imaging*. 2019;19(1):23. doi:10.1186/s12880-019-0321-9

28. Masokano IB, Liu W, Xie S, Marcellin DFH, Pei Y, Li W. The application of texture quantification in hepatocellular carcinoma using CT and MRI: a review of perspectives and challenges. *Cancer Imaging*. 2020;20(1):67. doi:10.1186/s40644-020-00341-y
29. Wang Q, Wang A, Wu X, et al. Radiomics models for preoperative prediction of the histopathological grade of hepatocellular carcinoma: a systematic review and radiomics quality score assessment. *Eur J Radiol*. 2023;166:111015. doi:10.1016/j.ejrad.2023.111015
30. Yu H, Touret AS, Li B, et al. Application of texture analysis on parametric T1 and T2 maps for detection of hepatic fibrosis. *J Magn Reson Imaging*. 2017;45(1):250–259. doi:10.1002/jmri.25328
31. Sun K, Shi L, Qiu J, et al. Multi-phase contrast-enhanced magnetic resonance image-based radiomics-combined machine learning reveals microscopic ultra-early hepatocellular carcinoma lesions. *Eur J Nucl Med Mol Imaging*. 2022;49(8):2917–2928. doi:10.1007/s00259-022-05742-8
32. Wu Y, Zhu M, Liu Y, et al. Peritumoral imaging manifestations on Gd-EOB-DTPA-enhanced MRI for preoperative prediction of microvascular invasion in hepatocellular carcinoma: a systematic review and meta-analysis. *Front Oncol*. 2022;12:907076. doi:10.3389/fonc.2022.907076
33. Zhao Y, Zhang J, Wang N, et al. Intratumoral and peritumoral radiomics based on contrast-enhanced MRI for preoperatively predicting treatment response of transarterial chemoembolization in hepatocellular carcinoma. *BMC Cancer*. 2023;23(1):1026. doi:10.1186/s12885-023-11491-0
34. Wang LL, Li JF, Lei JQ, et al. The value of the signal intensity of peritumoral tissue on Gd-EOB-DTPA dynamic enhanced MRI in assessment of microvascular invasion and pathological grade of hepatocellular carcinoma. *Medicine*. 2021;100:e25804. doi:10.1097/MD.0000000000025804
35. Xie XY, Chen R. Research progress of MRI-based radiomics in hepatocellular carcinoma. *Front Oncol*. 2025;15:1420599. doi:10.3389/fonc.2025.1420599
36. Wang F, Cheng M, Du B, et al. Predicting microvascular invasion in small (≤ 5 cm) hepatocellular carcinomas using radiomics-based peritumoral analysis. *Insights Imaging*. 2024;15:90. doi:10.1186/s13244-024-01649-0
37. Chong H, Gong Y, Pan X, et al. Peritumoral Dilation Radiomics of Gadoxetate Disodium-Enhanced MRI Excellently Predicts Early Recurrence of Hepatocellular Carcinoma without Macrovascular Invasion After Hepatectomy. *J Hepatocell Carcinoma*. 2021;8:545–563. doi:10.2147/JHC.S309570
38. Parikh ND, Mehta AS, Singal AG, Block T, Marrero JA, Lok AS. Biomarkers for the Early Detection of Hepatocellular Carcinoma. *Cancer Epidemiol Biomarkers Prev*. 2020;29(12):2495–2503. doi:10.1158/1055-9965.EPI-20-0005
39. Kim SJ, Jung CW, Anh NH, et al. Metabolic phenotyping combined with transcriptomics metadata fortifies the diagnosis of early-stage Hepatocellular carcinoma. *J Adv Res*. 2025;74:153–163. doi:10.1016/j.jare.2024.09.007